Clay Minerals, (2007) **42**, 109–128

Prograde epizonal clay mineral assemblages and retrograde alteration in tectonic basins controlled by major strike-slip zones (W Iberian Variscan chain)

M. VÁZQUEZ[1], I. ABAD[2,*], J. JIMÉNEZ-MILLÁN[2], F. T. ROCHA[1], P. E. FONSECA[3] AND H. I. CHAMINÉ[1,4]

[1] *Centro de Minerais Industriais e Argilas (MIA), Departamento de Geociências, Universidade de Aveiro, 3810-193 Aveiro, Portugal,* [2] *Departamento de Geología, Universidad de Jaén, Campus Universitario, Edificio B-3, 23071 Jaén, Spain,* [3] *Departamento de Geologia, Faculdade de Ciências da Universidade de Lisboa and LATTEX, Portugal,* [4] *Departamento de Engenharia Geotécnica, Instituto Superior de Engenharia do Porto (ISEP), Portugal*

(*Received 28 April 2006; revised 22 December 2006*)

ABSTRACT: We have carried out optical microscpy, X-ray diffraction (XRD) and scanning and transmission electron microscopy (SEM and TEM) studies of phyllosilicates from black slates of very low to low-grade metamorphism. Such slates belong to a Middle/Late Devonian basin and an Early Carboniferous basin associated with the Porto–Tomar–Ferreira do Alentejo strike-slip shear zone (Ossa-Morena Zone, Portuguese Iberian Variscan Massif). These black slates are imbricated in an Upper Proterozoic substratum of higher metamorphic grade. Kübler Index values of white micas and mineral assemblages deduced from the XRD, SEM and TEM data (muscovite, chlorite and pyrophyllite) indicate high anchizonal and epizonal metamorphic conditions for slates from these basins. The *b* parameter and the phengitic contents of mica suggest the occurrence of low pressures (1–2 kbar) related to an extensional geotectonic setting. The dense fracture network shown by SEM images and the high density of crystal defects revealed by the TEM study in the eastern basin, adjacent to faults produced by shearing, suggest that their epizonal phyllosilicates were more affected during deformation than those belonging to the western basin, favouring the development of a retrograde association (siderite, kaolin group minerals and Al-smectite) on the epizonal paragenesis. Microcavities formed along phyllosilicate cleavage acted as channels for fluid transport favouring alteration under low-temperature conditions.

KEYWORDS: TEM, SEM, shear deformation, Iberian Massif, muscovite, chlorite, dickite, kaolinite, retrograde alteration, low-*T* metamorphism.

The phyllosilicates are minerals that provide large amounts of information on very low and low-grade metamorphism, and therefore are useful in deciphering the processes involved from diagenesis to regional metamorphism. Merriman & Frey (1999) described specific patterns of very low-grade metamorphism that are essential to distinguish among various geotectonic settings in the absence of higher-grade metamorphic rocks. However, the establishment of metamorphic paths in very low and low-grade stratigraphic sequences is not an easy task as textural relations between minerals are not obvious; there are intergrowths of phases, and a general lack of equilibrium is characteristic (Nieto, 2002; Do Campo & Nieto, 2003).

* E-mail: miabad@ujaen.es
DOI: 10.1180/claymin.2007.042.1.08

The interaction between basin heat flow, tectonic stress, and the fluid pressure flow is the main factor responsible for the reaction progress of clay minerals in low-temperature environments (see Árkai *et al*., 2002; Robinson *et al*., 2002; Kemp *et al*., 2005, among others). Textural, structural and compositional features of phyllosilicates in tectonic basins formed by the activity of fault systems can provide essential information about the relative importance of these factors on the clay minerals' crystallization (Inoue *et al*., 2004; Schleicher *et al.*, 2006). In this research, we have carried out a detailed study of the phyllosilicates in Devonian and Carboniferous tectonic basins located in the Espinho–Albergaria-a-Velha metamorphic belt (northernmost domain of the Ossa-Morena Zone; Chaminé, 2000; Chaminé *et al.*, 2003a,b). These tectonic basins contain black slates of very low to low-grade metamorphism (Moço *et al.*, 2001). The very fine-grained texture of these rocks has made it necessary to examine them not only by scanning electron microscopy (SEM), using backscattered electron (BSE) imaging, but also by transmission electron microscope (TEM). We document the crystal-chemical parameters, compositions and textural relationships at a lattice scale of phyllosilicates. With all these data, we have tried to determine the influence of the shear deformation and the metasomatic/hydrothermal effects on the clay minerals' transformations and correlate the phyllosilicate features with the geodynamic context of these basins.

GEOLOGICAL FRAMEWORK AND MATERIALS

The NW border of the Iberian Massif is transected by a dextral wrench-fault, the Porto–Coimbra–Tomar shear zone (W Portugal). This major shear zone is a dextral strike-slip fault that acts as the boundary between two major zones of the Iberian Massif: the Portuguese northernmost domain of the so-called Ossa-Morena Zone and the Central-Iberian Zone (e.g. Lotze, 1945; Julivert *et al.*, 1974; Gama Pereira, 1987; Ribeiro *et al.*, 1990; Chaminé *et al.*, 2003b). The study areas are found in the western side of this mega-shear band and therefore belong to the Espinho−Albergaria-a-Velha metamorphic belt, Ossa-Morena Zone (Fig. 1). This crystalline polymetamorphosed belt of the Iberian Variscides is part of the Porto–Tomar–Ferreira do Alentejo major shear zone (Chaminé, 2000; Ribeiro *et al.*, 2003; Chaminé *et al.*, 2003a,b), and is enclosed within the Western Iberian Line (Chaminé *et al.*, 2003b).

Three types of tectonostratigraphic units can be distinguished in this region (Chaminé, 2000; Chaminé *et al.*, 2003a,b, 2006; Fernández *et al.*, 2003; Gomes *et al.*, 2006 and references therein):

(1) Thrusting allochthonous units of middle- to high-metamorphic grade, assumed of Upper Proterozoic/Cambrian times containing biotitic micaschist and migmatitic rocks;

(2) Autochthonous/parautochthonous Upper Proterozoic (Beetsma, 1995) tectonostratigraphic units of low- to high-grade metamorphic rocks, composed of garnetiferous black-greenish phyllites with interlayered amphibolites, garnet-staurolite micaschist and gneissic rocks;

(3) Units with Middle-Upper Palaeozoic black slates that are interbedded in laminated siltstones with interlayered metacarbonates (Fernandes *et al.*, 2001). As result of tectonic and sedimentary procceses, these units are overhung and imbricated with the units b, which form the substratum where these materials were deposited in Middle/Late Devonian and Early Carboniferous basins. The basins were formed on this substratum in either transpressional or transtensional areas associated with the Porto–Coimbra–Tomar dextral strike-slip shear zone. The continuous action carried after this megastructure out the imbrication of the previously described tectonostratigraphic units. The formation of transtensional areas by the occurrence of offsets and bifurcations in strike-slip fault systems produced N-S to NNW−SSE tectonic basins. These basins are composed of Upper Palaeozoic sequences containing black slates of very low- to low-grade metamorphism that contrast with the country rock substratum. These metasedimentary rocks have been observed along a strip subparallel to the major shear zone (Chaminé *et al.*, 2003b, 2006). The metapelitic units are obscured mainly by Meso-Cenozoic cover deposits from the Lusitanian Basin (Oliveira *et al.*, 2002).

This study is focused on the Middle-Upper Palaeozoic black slates from two tectonic basins associated with the Porto–Coimbra–Tomar shear zone, which are located within the Albergaria-a-Velha–Águeda area (Fig. 1). The western basin is >2 km from the major fault zone and contains Early Carboniferous black slates characterized by a rather constant foliation dip. By contrast, the eastern basin is limited by important faults of the shear zone. The

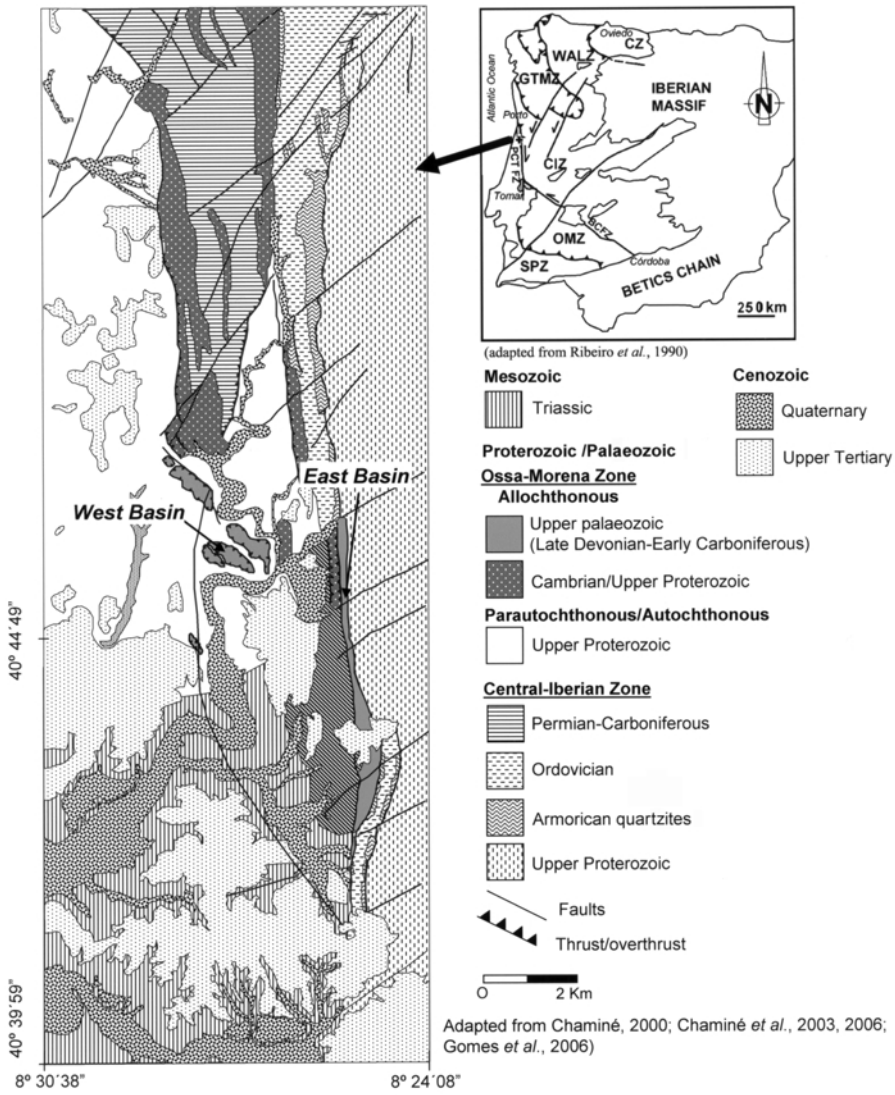

FIG. 1. Geographical and geological location of the studied basins. Regional geotectonic framework of the Albergaria-a-Velha–Águeda area in the Porto–Coimbra–Tomar shear zone, Ossa-Morena Zone, NW Portugal (adapted from Chaminé, 2000; Chaminé *et al.*, 2003, 2006; Gomes *et al.*, 2006). Explanation: CZ: Cantabrian Zone, WALZ: Western Asturian-Leonese Zone, GTMZ: Galicia-Trás-os-Montes Zone, CIZ: Central-Iberian Zone, OMZ: Ossa-Morena Zone, SPZ: South Portuguese Zone, PCTFZ: Porto–Tomar shear zone, BCFZ: Badajoz–Córdoba shear zone.

materials from this basin (correlated to Late Devonian black slates in this area; Fernandes *et al.*, 2001) have important changes of the foliation dip, showing a chaotic or melange aspect. Moreover, these slates have some injections of interbedded metasomatic carbonate rocks and black greywacke lenses. Some of the studied rocks from the eastern basin adjacent to the fault that borders this basin (see Table 1) can be considered as phyllonites of moderate deformation. These samples develop a slaty cleavage mainly defined by phyllosilicates and elongated quartz according to the stretching direction. Chaotic zones and sigmoidal quartz crystals can be observed.

TABLE 1. Crystal-chemical parameters and bulk mineralogy.

	White mica					Chlorite			Mineral composition
	*d*002 Å		*b* Å	Illite crystallinity' (KI) CIS' scale Δº2θ		*d*001 Å		*b* Å	Qtz, Pl, K-white mica, Chl
Samples	<2 μm	bulk		<2 μm	bulk	<2 μm	bulk		(all the samples)
Eastern basin									
ST5	9986	10005	8991	0.14	0.17	14.11	14.13	9277	Kfs, Kln
ST8	9984	10000	9011	0.23	0.13	14.13	14.15	9251	Kln, Fe-ox., Ilm, Rt, Tur, Ap
ST9	9996	9992	8977	0.22	0.19	14.15	14.13	9254	Kln, Ill-Pg, Fe-ox., Ilm, Rt, Tur, Ap
ST10*	9994	9994	9015	0.18	0.16	14.13	14.15	9252	Kln, Sd
ST13*	9982	9984	–	0.34	0.32	14.14	–	–	Kln, Chl-Vrm
ST16	9991	9994	8973	0.22	0.20	14.13	14.13	9311	Kfs
ST17	9990	9999	8995	0.21	0.23	14.12	14.14	9313	Kln
ST19*	9993	9984	8991	0.18	0.16	14.13	14.14	9253	Kln, Chl-Sm
ST20	9987	9985	8993	0.22	0.18	–	14.13	9252	Kln, Chl-Sm
Western basin									
SV6	9996	9992	8993	0.18	0.15	14.13	14.15	9306	Kfs, Prl, Fe-ox., Ilm, Rt, Tur, Ap
SV7	9992	9990	8999	0.25	0.15	14.14	14.13	9313	Kfs
SV8	9989	9990	–	0.27	0.18	14.12	14.12	–	Kfs
SV9	9994	9992	8990	0.22	0.18	14.13	14.13	9302	Kfs, Fe-ox., Ilm, Rt, Tur, Ap
SV10	9988	9995	8967	0.20	0.16	14.13	14.13	9302	Kfs
SV11	9992	9901	–	0.21	0.13	14.13	14.13	9314	
SV12	9992	9992	8995	0.23	0.17	14.13	14.13	9315	Kfs, Ap, Sd
SV13	9999	9994	8986	0.29	0.16	14.13	14.13	9303	Kfs
SV14	9994	9999	8981	0.24	0.15	14.13	14.13	9304	
SV15	9994	9994	8978	0.25	0.18	14.13	14.13	9317	Kfs
SV16	9.90	9992	8978	0.23	0.17	14.13	14.13	9304	Kfs
SV17	9990	9990	9001	0.18	0.17	14.14	14.13	9313	Kfs, Fe-ox., Ilm, Rt, Tur, Ap, Vrm

Mineral abbreviations according to Kretz (1983), Ill-Pg = Na-K mica, Fe-ox.= Fe oxide, Sm = smectite
The high- and low-grade boundaries of the anchizone in the 'CIS' scale are 0.295 and 0.49−0.50Δº2θ (Kish *et al*., 2004)
* Samples taken less than 20 m away from the faults that border the basin. The rest of samples are not directly related to any fault.

I'm inclined not to believe that 9.90!

ANALYTICAL METHODS

X-ray diffraction

Unaltered samples of slates were carefully collected, in order to minimize the effects of weathering. Samples were washed and, after coarse crushing, homogeneous rock chips were used for preparation of samples for XRD. Whole-rock samples and clay fraction (<2 μm) were studied using a Philips PW 1710 X-ray diffractometer Cu-κα radiation, graphite monochromator and automatic divergence slit at the Departamento de Mineralogía y Petrología of the Universidad de Granada (Spain) and a Philips X'Pert PW 3040/60 powder diffractometer with Cu-$K\alpha$ radiation at the Universidade de Aveiro (Portugal). The <2 μm fractions were separated by repeated extraction of supernatant liquid subsequent to settling. Oriented aggregates were prepared by sedimentation on glass slides. Ethylene-glycol (EG) treatment was carried out on some samples to corroborate the identification of smectite and/or chlorite-smectite mixed-layers. Several samples were collected for studying the possible presence of dickite. Vein areas were hand-picked for analyses in order to minimize the inclusion of impurities. The kaolinite polytype was determined by XRD, according to Bailey (1980). Preparations of samples and experimental conditions for illite 'crystallinity' (Kübler Index, KI) measurements were carried out according to IGCP 294 IC Working Group recommendations (Kisch, 1991). Our KI measurements (y) were transformed into C.I.S. values (x) according to the equation $y = 1.897x + 0.113$ ($r = 0.995$), obtained in the laboratory using the inter-laboratory standards of Warr & Rice (1994). The KI values were measured for the <2 μm fractions and for the bulk-rock samples. The b cell parameters of micas and chlorites were obtained from the 060 peaks measured on slices of rock cut normal to the sample foliation. For all spacing measurements, quartz from the sample itself was used as the internal standard. In this work, we have also made a simple qualitative estimate of the existence of illite polytypes by comparing the $1M_d$ 112 and $2M_1$ 025 reflections according to the method proposed by Caillere *et al.* (1982).

Electron microscopy

Following the XRD and optical studies, representative samples were selected for electron microscopy study on the basis of the KI values and the mineral assemblages. Carbon-coated slices were examined by SEM, using BSE imaging and energy-dispersive X-ray (EDX) analysis in order to obtain textural and chemical data. These observations were carried out using a Zeiss DSM 950 SEM, equipped with an X-ray Link Analytical QX-20 energy-dispersive X-ray system (EDX) at the Centro de Instrumentation Científica (C.I.C.) of the Universidad de Granada. An accelerating voltage of 20 kV, with a beam current of 1−2 nA and counting time of 100 s per step were used to analyse the phyllosilicates by SEM, using both natural and synthetic standards: albite (Na), periclase (Mg), wollastonite (Si and Ca), and orthoclase (K), and synthetic Al_2O_3 (Al), Fe_2O_3 (Fe) and $MnTiO_3$ (Ti and Mn).

Due to the very fine-grained nature of these samples, the spatial resolution of the textural features obtained using the optical and SEM microscopes was not enough to characterize all the textural features. Therefore, two samples representative of these basins were selected for HRTEM study using a Philips CM20 (STEM) located at C.I.C. and equipped with an EDX solid-state detector, operating at 200 kV, with a

Fig 2 not referred,

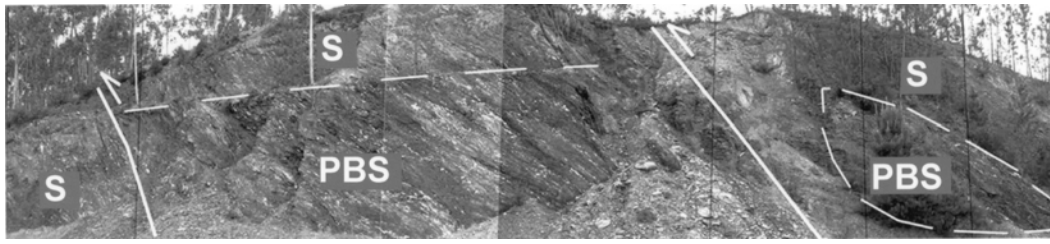

FIG. 2. Palaeozoic black shales (PBS) imbricated with the tectonostratigraphic units of the substratum (S) by the interaction of tectonic and sedimentary processes.

LaB_6 filament and a spatial resolution of 2.7 Å between points and 1.4 Å between fringes.

The structural formulae of micas were calculated on the basis of 22 negative charges O_{10} $(OH)_2$. Although these analytical techniques cannot distinguished between Fe^{3+} and Fe^{2+}, Guidotti *et al.* (1994) showed that the opaque-mineral assemblage (hematite) can be used to estimate the Fe^{3+}/Fe^{2+} ratio in muscovite. Even in low redox-potential parageneses, ~50% of the Fe in muscovite is Fe^{3+}, and values close to 85 % can be reached in less reducing environments. Therefore, in the calculations of formulae it has been assumed that 75% of the Fe in the micas is Fe^{3+}.

Infrared spectroscopy

Dickite can be easily distinguished from other kaolin polytypes using IR spectroscopy. The IR spectra of samples with kaolin-group minerals were recorded with a Nicolet 20SXB FTIR spectrometer at C.I.C. (Universidad de Granada) over the range 4000−400 cm^{-1} (resolution of 0.5 cm^{-1}) using wafers with 2 mg of sample and 200 mg of KBr each.

Chemical analyses of rocks

Whole-rock analyses of the major elements of selected samples were carried out using X-ray fluorescence (XRF) in a Philips PW 1040/10 spectrometer at the C.I.C. (Universidad de Granada).

RESULTS

The characterization of samples by XRD and electron microscopy techniques (SEM/EDX and TEM/AEM – analytical electron microscopy) shows that quartz, white mica, chlorite and plagioclase are the principal phases in all samples. Moreover, K-feldspar, pyrophyllite and kaolin among others, were detected only in some samples. Accessory minerals include Fe oxides, siderite, rutile, ilmenite and apatite (Table 1).

XRD mineralogy and crystal-chemical parameters

In both basins, the basal spacing of the mica is ~9.99 Å (σ = 0.01) and varies with no clear trend throughout the sequences. An overall average of 8.991 Å (σ = 0.014) has been obtained for the *b* cell parameter (Table 1). The illite 'crystallinity' results (Table 1) indicate that all the studied samples fall in the ranges of very low and low-grade metamorphism (0.34 to 0.14Δº2θ) corresponding to anchizonal and epizonal grades (according to Merriman & Peacor, 1999). We have not observed significant differences among the range of 'illite crystallinity' values determined in samples from the western basin and those from the eastern basin. The illite polytype study shows that the $2M_1$ polytype is predominant, revealing the absence of differences for the population of polytypes between both basins.

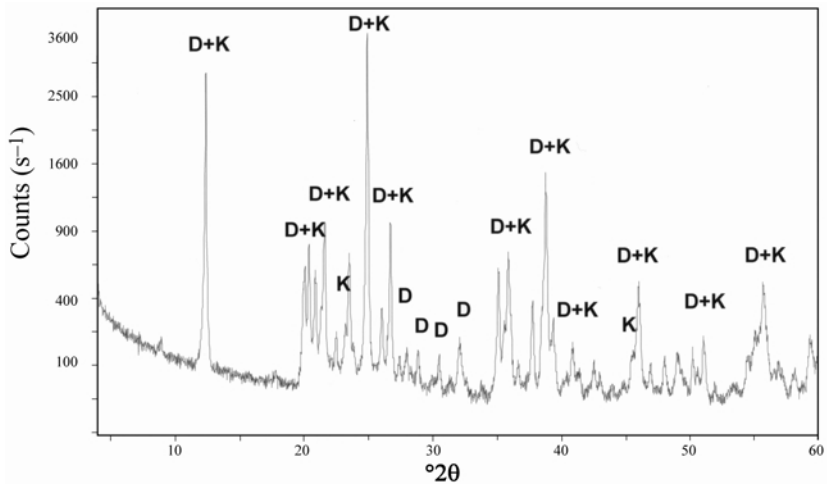

FIG. 3. XRD diagram which shows the presence of dickite (D) and kaolinite (K) in an East basin sample (ST-8).

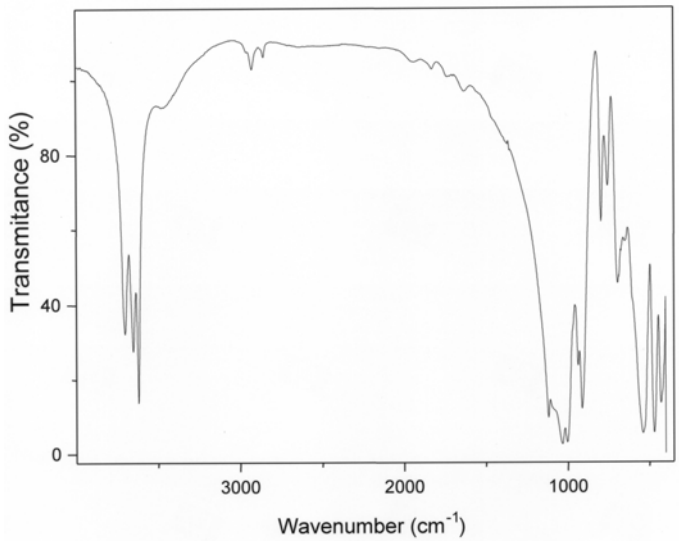

FIG. 4. IR spectrum of dickite in an East basin sample (ST-8).

A narrow peak at 14 Å of chlorite occurred both before and after glycolation in the western basin samples, indicating that there are no detectable mixed-layer expandable components. In the eastern basin slates, the chlorite has wide and poorly defined reflection peaks at 14 Å, reflecting low quantities and poor 'crystallinity'. Nevertheless, interstratified chlorite-smectite and chlorite-vermiculite have been detected in some of these rocks. Ethylene glycol solvation of chlorite-smectite caused the appearance of the 004 reflection at about 11.5º2θ and a broadening of the 003 and 004 reflections, while the heating at 300ºC caused the shift to 12 Å of the 14 Å reflection on the aggregates. The chlorite-vermiculite was identified by the extent of expansion when treated with EG and by heat treatments (14 Å reflection collapsed to 12 Å). The crystal-chemical parameters of chlorites show a rather homogenous basal spacing (average = 14.13 Å and σ = 0.01) while the *b* parameter is slightly smaller in the eastern basin samples (9.274 Å) than in the western basin chlorites (9.309 Å).

In addition, kaolinite and dickite appear only in the eastern basin samples. Dickite has been found in veins and kaolinite in veins and in the rock matrix. According to Bailey (1980), the XRD data of vein samples from the eastern basin (Fig. 3) show the presence of some characteristic reflections of dickite such as 3.26, 3.10, 2.94 and 2.80 Å. However, we have also detected some kaolinite reflections such as 3.84 and 1.99 Å, showing some contamination of kaolinite in dickite samples. The IR spectrum obtained for these samples is similar to the dickite reference spectrum given by Farmer (1974) over the whole frequency range. In particular, the three bands at ~3710, 3655 and 3620 cm^{-1} are characteristic of dickite (Fig. 4).

Electron microscopy observations (SEM and TEM)

Textural aspects. Back-scattered electron images of samples from the western basin reveal the presence of microdomains up to 50 µm thick where a poorly developed phyllosilicate matrix made of small size chlorite and muscovite flakes anastomosing angular grains of albite and quartz (Fig. 5a). These domains are limited by microbands with a more developed parallel texture of phyllosilicates. Muscovite and chlorite intergrowths can be observed in these microbands. Samples from the eastern basin show a well developed crenulation cleavage which favoured the concentration of quartz in the hinges and muscovite in the fold limbs (Fig. 5b). Some open spaces in the fold hinges are filled by kaolin. Quartz grains in fold limbs can develop sigmoid forms. Moreover, a vein network that commonly follows the orientation defined by the muscovite crystals is well developed. However, some veins cross-cutting this orientation are aslo observed. Veins are mainly filled by

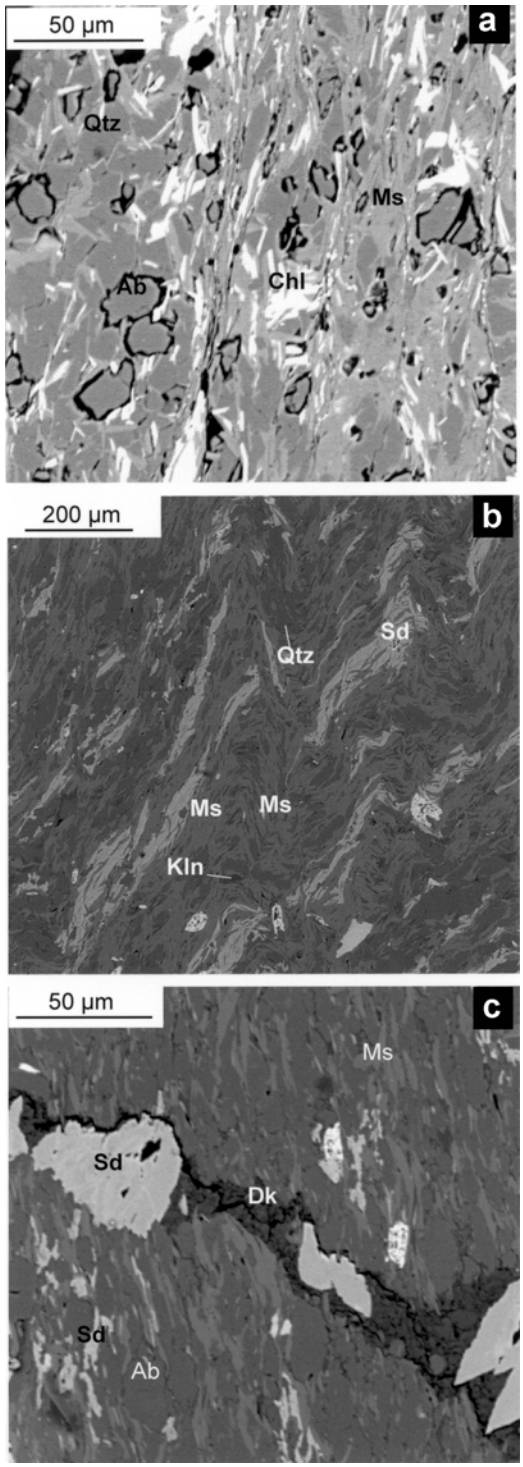

siderite, although randomly oriented aggregates of dickite flakes (according to the XRD data) can also appear as filling material (Fig. 5c).

Low-magnification images and AEM analyses of samples from the western basin reveal the presence of thick phyllosilicate grains (>1 μm) consisting primarily of alternating muscovite, pyrophyllite, chlorite and kaolin (see Tables 3 and 4).

The electron diffraction (SAED) images of samples from the western basin show that muscovite is intergrown with pyrophyllite and kaolin. Figure 6a shows that the c^* of kaolin is parallel to c^* of muscovite, and they form a low angle with c^* of the 9 Å phase. Micaceous grains mainly consist of thick packets of well crystallized muscovite (>500 Å), although beam-damage mottling is commonly developed (Fig. 6b). The TEM images obtained do not provide information about the types of mica polytype that are present in these samples. Some intergrown areas of kaolinitic composition without lattice fringes is observed.

Chlorite grains from the western basin samples are quite homogeneous, and we observed no alteration effects. In the high-resolution images, $(001)_{chl}$ of 14 Å lattice fringes form regular sequences up to 1 μm thick (Fig. 6c). The TEM images and SAED patterns demonstrate that chlorite is well crystallized and has few defects. Some diffraction images indicate that chlorite is intergrown with a phyllosilicate of d_{001} = 10 Å (Fig. 6d). The SAED patterns of chlorite generally exhibit sharp and intense reflections without streaking along c^*. Figure 6d shows that c^* of chlorite is not parallel to c^* of the 10 Å phase. The HRTEM images from these areas reveal the presence of chlorite packets with 14 Å layers and muscovite packets with 10 Å layers the lattice fringes of which form an angle of ~10º (Fig. 6e). Both packets are separated by an electron beam-damaged packet of Al smectite (see Table 4).

The TEM study of the samples from the eastern basin has allowed us to recognize the presence of well developed grains of muscovite and chlorite as

FIG. 5. BSE images showing the textures of the samples. (a) Microdomains of phyllosilicates with low deformation (West basin). (b) Crenulation cleavage, which favoured the concentration of quartz in the hinges and of muscovite in the fold limbs (East basin). (c) Dickite and siderite filling fractures (East basin). Mineral abbreviations according to Kretz (1983).

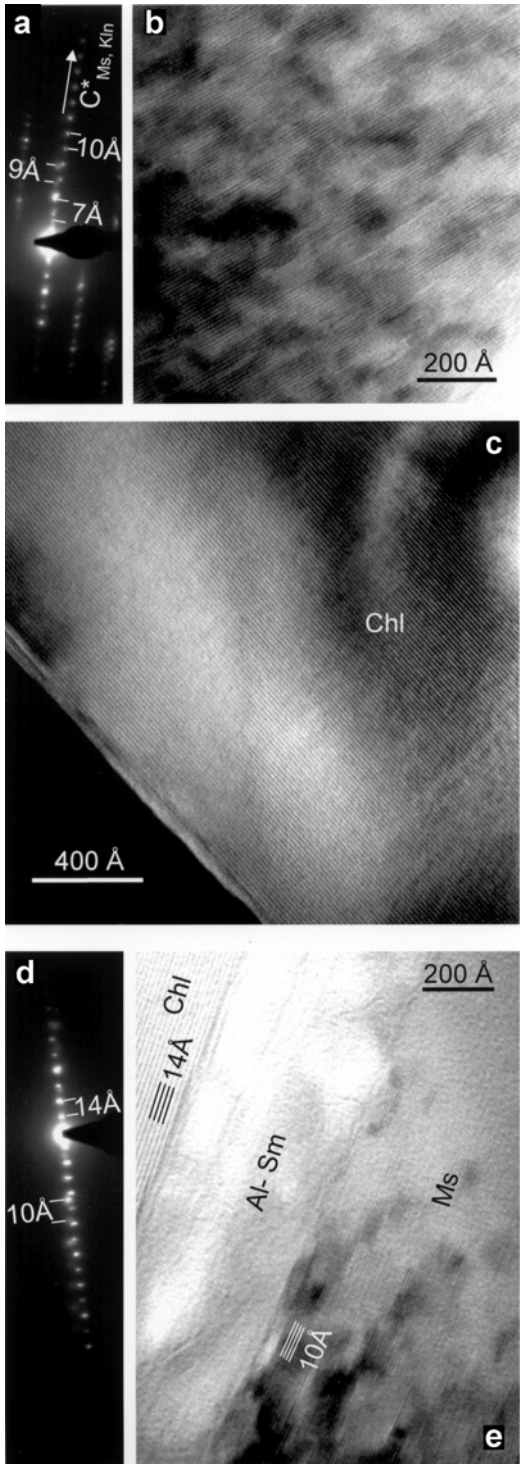

well as some poorly crystalline aggregates of phyllosilicates. The SAED images obtained from muscovite packets indicate that a two-layer polytype is predominant (Fig. 7a). Muscovite packets are commonly characterized by the formation of numerous elongated gaps. These muscovite packets display an intense mottled appearance consisting of blocky patches and irregular areas of darker contrast (Fig. 7a). Mottling distribution is oblique to the (001) basal planes. In some HRTEM images, low-angle boundaries among thin micropackets of muscovite (Fig. 7a) are also observed. Dislocations and layer disruption are commonly found (Fig. 7b). As in the western basin, muscovite packets also contain packets of beam-damaged kaolin. In some cases, kaolin is the predominant phyllosilicate and muscovite only appears as relict thin packets (<100 Å) with 10 Å fringes that show fanned-out texture and are intergrown with electron beam-damaged areas (Fig. 7c). In very few packets, kaolin develops lattice-fringe resolution, allowing us to observe that, according to the SAED pattern, fringes of kaolin and muscovite are parallel to each other and to the boundary between packets (Fig. 7b). We have not observed 7 Å layers within the muscovite packets.

Chlorite crystals of the eastern basin slates are more affected by layer bending and deformation than the chlorite from the western basin. Lattice fringes from hinge zones of bent packets of chlorite (Fig. 7d) are frequently disrupted and imbricated. An evolution from fairly ordered and almost undeformed chlorite packets, (in which lattice fringe images reveal the presence of scarce 10 and 7 Å fringes amongst the homogeneous dominant 14 Å fringes – see Fig. 7e), to bent, broken and altered chlorite with irregular edges containing aggregates of poorly crystalline material along the cleavage planes has been recognized (Fig. 7d). The texture of these minerals varies from aggregates made of completely unoriented packets

FIG. 6. TEM images of phyllosilicates from the western basin samples. (a) SAED pattern of muscovite intergrown with pyrophyllite and kaolinite. (b) Mottled distribution in well crystallized mica packets. (c) Homogeneous chlorite grain with a regular sequence of 14 Å lattice fringes. (d) SAED pattern of chlorite intergrown with muscovite. (e) HRTEM image showing a chlorite packet and a muscovite packet separated by an Al-smectite packet. Mineral abbreviations according to Kretz (1983).

~100–400 Å thick (Fig. 7f) to semi-ordered aggregates of partially oriented packets up to 400 Å thick (Fig. 7g). Combination of the AEM, SAED patterns and HRTEM images suggests that these aggregates include kaolin, Al-smectite and fine-grained muscovite. Kaolin can be recognized by the 7 Å diffraction of the SAED images and the presence of AEM analyses contaminated with an Al-rich phase. Fine-grained muscovite and smectite packets are beam damaged and do not show 10 Å lattice fringes but in some scarce packets of muscovite a periodicity of 20 Å can be recognized which is characteristic of a two-layer polytype (Fig. 7h).

Chemical characterization of phyllosilicates

The structural formulae of K-rich dioctahedral micas corresponding to both basins are presented in Tables 2 and 3. Eastern basin micas are characterized by greater Si and (Fe + Mg) contents (Si average = 3.21 a.p.f.u., Fe + Mg average = 0.28 a.p.f.u.) than those of the western basin micas (Si = 3.11 a.p.f.u., Fe + Mg = 0.16 a.p.f.u.). In western basin slates the Al content in micas is greater (Al average = 2.73 a.p.f.u.) than in eastern basin rocks (Al average = 2.49 a.p.f.u.). The interlayer charge populations range from 0.8 to 1.0 a.p.f.u. These features can be

TABLE 2. Structural formulae* for K-rich dioctahedral micas on the basis of SEM data.

	Si	^{IV}Al	^{VI}Al	Fe	Mg	Ti	$^{VI}\Sigma$	K	Na	Σinter.	Al tot	Fe+Mg
Western basin												
SV6/9/1	3.10	0.90	1.82	0.09	0.08	0.02	2.01	0.85	0.10	0.95	2.72	0.16
SV6/9/2	3.14	0.86	1.84	0.10	0.07	0.01	2.01	0.78	0.11	0.89	2.70	0.16
SV6/9/3	3.12	0.88	1.83	0.11	0.09	0.01	2.05	0.81	0.03	0.84	2.71	0.20
SV6/9/4	3.06	0.94	1.73	0.16	0.13	0.02	2.05	0.85	0.08	0.93	2.67	0.30
SV6/11/1	3.07	0.93	1.89	0.07	0.06	0.01	2.03	0.80	0.12	0.92	2.82	0.13
SV6/11/2	3.10	0.90	1.85	0.08	0.07	0.02	2.02	0.85	0.08	0.92	2.75	0.15
SV6/11/3	3.04	0.96	1.79	0.16	0.09	0.02	2.06	0.81	0.08	0.89	2.75	0.25
SV6/12/3	3.10	0.90	1.85	0.07	0.06	0.02	2.00	0.84	0.10	0.94	2.76	0.13
SV6/12/7	3.08	0.92	1.88	0.08	0.03	0.01	2.00	0.86	0.11	0.97	2.80	0.11
SV6/13/2	3.09	0.91	1.85	0.08	0.07	0.01	2.02	0.83	0.11	0.94	2.76	0.15
SV6/14/1	3.11	0.89	1.84	0.08	0.08	0.02	2.01	0.84	0.09	0.93	2.73	0.16
SV7/1/1	3.07	0.93	1.89	0.06	0.04	0.01	2.02	0.83	0.09	0.92	2.82	0.10
SV7/1/2	3.14	0.86	1.85	0.07	0.07	0.01	2.00	0.85	0.11	0.95	2.71	0.14
SV7/1/4	3.10	0.90	1.89	0.05	0.04	0.01	1.99	0.85	0.11	0.97	2.79	0.09
SV7/1/5	3.08	0.92	1.83	0.10	0.07	0.02	2.03	0.82	0.10	0.92	2.75	0.17
SV7/2/1	3.06	0.94	1.85	0.09	0.09	0.01	2.04	0.84	0.09	0.93	2.79	0.17
SV7/2/2	3.13	0.87	1.79	0.12	0.10	0.01	2.02	0.85	0.07	0.93	2.66	0.22
SV7/2/4	3.06	0.94	1.92	0.05	0.05	0.01	2.03	0.78	0.14	0.92	2.86	0.10
SV7/3/1	3.06	0.94	1.87	0.06	0.06	0.02	2.02	0.85	0.09	0.95	2.81	0.12
SV7/3/3	3.09	0.91	1.87	0.06	0.06	0.01	2.01	0.82	0.11	0.95	2.79	0.12
SV7/3/4	3.14	0.86	1.83	0.08	0.08	0.01	2.00	0.86	0.09	0.95	2.69	0.15
SV7/5/2	3.24	0.76	1.85	0.06	0.09	0.01	2.01	0.82	0.03	0.85	2.61	0.15
SV7/5/3	3.22	0.78	1.84	0.06	0.11	0.00	2.01	0.83	0.04	0.88	2.62	0.17
SV9/1/1	3.09	0.91	1.85	0.08	0.08	0.01	2.02	0.74	0.20	0.94	2.76	0.16
SV9/2/1	3.13	0.87	1.84	0.08	0.08	0.01	2.01	0.82	0.11	0.93	2.71	0.17
SV9/2/5	3.11	0.89	1.81	0.11	0.08	0.01	2.01	0.81	0.12	0.95	2.70	0.19
SV9/2/6	3.07	0.93	1.63	0.30	0.15	0.01	2.09	0.75	0.12	0.86	2.56	0.45
SV9/3/1	3.17	0.83	1.84	0.07	0.07	0.02	1.99	0.82	0.11	0.93	2.67	0.14
SV9/3/2	3.07	0.93	1.85	0.08	0.07	0.02	2.02	0.85	0.09	0.94	2.77	0.16
SV9/5/1	3.12	0.88	1.89	0.04	0.06	0.01	2.00	0.86	0.07	0.93	2.77	0.10
SV9/5/4	3.07	0.93	1.95	0.03	0.01	0.01	2.00	0.68	0.24	0.93	2.88	0.04
SV9/5/1	3.13	0.87	1.91	0.04	0.06	0.01	2.01	0.73	0.14	0.89	2.78	0.09
SV9/5/2	3.08	0.92	1.93	0.03	0.02	0.01	1.99	0.70	0.24	0.96	2.85	0.05
SV9/5/4	3.09	0.91	1.78	0.15	0.10	0.02	2.05	0.81	0.07	0.89	2.70	0.24
SV17/1/2	3.40	0.60	1.82	0.05	0.06	0.01	1.94	0.78	0.05	0.84	2.42	0.11
SV17/3/2	3.16	0.84	1.84	0.10	0.06	0.01	2.00	0.83	0.08	0.91	2.68	0.16
SV17/4/1	3.10	0.90	1.88	0.05	0.04	0.02	1.98	0.92	0.06	0.99	2.78	0.09

Table 2 (*cont.*)

	Si	^{IV}Al	^{VI}Al	Fe	Mg	Ti	$^{VI}\Sigma$	K	Na	Σinter.	Al tot	Fe+Mg
Eastern basin												
ST81/1/2	3.26	0.74	1.70	0.12	0.15	0.03	2.00	0.88	0.01	0.90	2.44	0.13
ST81/2/5	3.17	0.83	1.69	0.15	0.15	0.03	2.03	0.91	0.00	0.91	2.52	0.30
ST81/3/1	3.13	0.87	1.76	0.11	0.11	0.03	2.00	0.93	0.04	0.97	2.63	0.22
ST81/3/2	3.29	0.71	1.70	0.12	0.14	0.02	1.99	0.86	0.04	0.90	2.41	0.26
ST81/3/3	3.23	0.77	1.73	0.11	0.12	0.03	1.98	0.89	0.06	0.95	2.50	0.23
ST81/4/3	3.18	0.82	1.73	0.13	0.13	0.03	2.01	0.91	0.02	0.93	2.56	0.25
ST81/5/1	3.30	0.70	1.72	0.10	0.12	0.02	1.97	0.79	0.13	0.93	2.42	0.22
ST81/5/3	3.13	0.87	1.54	0.26	0.23	0.04	2.06	0.92	0.03	0.95	2.40	0.48
ST81/5/4	3.15	0.85	1.46	0.33	0.27	0.03	2.08	0.82	0.09	0.91	2.31	0.60
ST81/6/2	3.11	0.89	1.81	0.09	0.08	0.03	2.00	0.94	0.02	0.96	2.71	0.16
ST9/1/1	3.14	0.86	1.76	0.11	0.12	0.03	2.02	0.90	0.02	0.92	2.62	0.24
ST9/1/2	3.15	0.85	1.79	0.10	0.10	0.02	2.01	0.91	0.04	0.94	2.64	0.20
ST9/1/3	3.21	0.79	1.73	0.11	0.11	0.03	1.98	0.92	0.03	0.96	2.52	0.22
ST9/1/4	3.20	0.80	1.70	0.14	0.15	0.03	2.01	0.91	0.02	0.93	2.50	0.28
ST9/3/1	3.24	0.76	1.71	0.11	0.16	0.03	2.00	0.91	0.00	0.91	2.47	0.27
ST9/3/6	3.42	0.58	1.66	0.14	0.15	0.02	1.97	0.81	0.01	0.83	2.24	0.29
ST9/4/3	3.34	0.66	1.69	0.12	0.14	0.02	1.97	0.84	0.03	0.88	2.35	0.26
ST9/5/3	3.26	0.74	1.49	0.24	0.23	0.08	2.05	0.80	0.01	0.82	2.24	0.47
ST9/5/4	3.17	0.83	1.67	0.19	0.17	0.03	2.06	0.85	0.00	0.85	2.50	0.35
ST9/5/5	3.15	0.85	1.72	0.12	0.17	0.03	2.03	0.91	0.02	0.93	2.57	0.29
ST9/5/6	3.20	0.80	1.69	0.13	0.15	0.03	1.99	0.94	0.03	0.97	2.49	0.27
ST9/6/1	3.18	0.82	1.74	0.11	0.14	0.03	2.02	0.91	0.00	0.91	2.56	0.25
ST10/2/3	3.20	0.80	1.71	0.13	0.13	0.03	1.99	0.95	0.00	0.95	2.51	0.26
ST10/3/1	3.16	0.84	1.69	0.15	0.15	0.02	2.01	0.97	0.00	0.97	2.53	0.30
ST10/6/4	3.18	0.82	1.69	0.13	0.14	0.04	2.00	0.96	0.01	0.97	2.51	0.27
ST10/8/4	3.22	0.78	1.70	0.13	0.14	0.03	2.00	0.94	0.00	0.94	2.48	0.27

TABLE 3. Structural formulae* for phyllosilicates on the basis of AEM data.

Analyses	Si	^{IV}Al	^{VI}Al	Fe	Mg	Ti	$^{VI}\Sigma$	K	Na	Σinter.	Al tot	Fe+Mg
K-rich dioctahedral micas (1)												
SV6/4a	3.12	0.88	1.87	0.05	0.11	0.00	2.03	0.76	0.14	0.90	2.75	0.16
SV6/5	3.12	0.88	1.84	0.07	0.11	0.00	2.02	0.76	0.18	0.94	2.73	0.18
Pyrophyllite (1)												
SV6/19	3.88	0.12	1.91	0.00	0.10	0.00	2.02	0.05	0.12	0.17	2.03	0.10

	Si	Al^{VI}	Fe	Mg	$^{VI}\Sigma$	K	Na	Σinter.
Kaolinite (2)								
SV6/8	4.03	3.77	0.04	0.09	3.90	0.11	0.13	0.24
SV6/13	4.10	3.66	0.09	0.07	3.81	0.15	0.09	0.24

	Si	Al^{IV}	Al^{VI}	Fe	Mg	Ti	$^{VI}\Sigma$	Ca	K	Na	Σinter.	Al tot
Al-smectite (1)												
ST13/5	3.78	0.22	1.60	0.19	0.21	0.00	1.99	0.00	0.33	0.12	0.45	1.82
ST13/6	3.62	0.38	1.76	0.07	0.21	0.00	2.04	0.03	0.21	0.19	0.43	2.15

* (1) normalized to $O_{10}(OH)_2$; (2) normalized to O_{10} $(OH)_8$

TABLE 4. SEM and AEM data for chlorites normalized to $0_{10}(OH)_8$.

	Si	^{IV}Al	^{VI}Al	Fe	Mg	Mn	Ti	$^{VI}\Sigma$	Fe/(Fe+Mg)
					SEM/EDX				
Western basin									
SV6/1/1	2.71	1.29	1.71	2.60	1.44	0.04	0.01	5.78	0.64
SV6/6/1	2.57	1.43	1.47	2.91	1.54	0.05	0.00	5.98	0.65
SV7/2/3	2.56	1.44	1.41	3.00	1.56	0.03	0.00	6.01	0.66
SV7/4/1	2.69	1.31	1.53	2.75	1.56	0.03	0.01	5.88	0.64
SV7/5/6	2.66	1.34	1.51	3.03	1.34	0.04	0.00	5.92	0.69
SV9/1/4	2.79	1.21	1.65	2.65	1.42	0.04	0.01	5.77	0.65
SV9/4/1	2.61	1.39	1.47	2.98	1.47	0.04	0.00	5.96	0.67
SV17/1/1	2.54	1.46	1.31	3.30	1.45	0.00	0.00	6.07	0.69
SV17/3/1	2.58	1.42	1.35	3.25	1.42	0.00	0.00	6.03	0.70
SV17/4/2	2.61	1.39	1.44	3.27	1.25	0.00	0.00	5.97	0.72

	Si	^{IV}Al	^{VI}Al	Fe	Mg	$^{VI}\Sigma$	Al tot	Fe/(Fe+Mg)
				TEM/AEM				
Western basin								
SV6/16	2.52	1.48	1.54	2.73	1.70	5.97	3.02	0.62
SV6/17	2.54	1.46	1.45	2.78	1.78	6.01	2.90	0.61
SV6/21	2.58	1.42	1.62	2.56	1.72	5.90	3.04	0.60
SV6/2	2.59	1.41	1.63	2.59	1.67	5.89	3.05	0.61
Eastern basin								
ST13/9	2.76	1.24	1.26	1.99	2.74	5.99	2.50	0.42
ST13/10	2.60	1.40	1.20	2.16	2.74	6.10	2.60	0.44
ST13/16	2.65	1.35	1.25	2.43	2.36	6.05	2.60	0.51
ST13/17	2.71	1.29	1.27	2.01	2.73	6.01	2.56	0.42

observed in Fig. 8, which shows that each chemical parameter is affected by several compositional vectors. The proportions of Si, Al and Fe + Mg are mostly controlled by the phengitic vector and to a lesser extent by the ferrimuscovitic vector. The ferrimuscovitic vector produces some greater Fe contents and lesser Al contents than expected as a result of phengitic substitution. In any case, although the phengitic content is low in both basins, eastern basin micas are more phengitic than western basin ones that show compositions nearer to the theoretical muscovite composition (grey disks in Fig. 8). Although all data plotted mainly along the muscovite-phengite line, the value ranges corresponding to each basin almost do not overlap (Fig. 8b,c,d).

No correlation between the interlayer population and Si exists ($r = -0.45$) which means an almost complete lack of illitic substitution. In fact, the data do not fit the theoretical line representing this compositional vector as the Si content is affected by

FIG. 7 (*facing page*). TEM images of phyllosilicates from the eastern basin samples. (a) Mottled 2*M* muscovite packet with elongated gaps and low-angle boundaries among micropackets. (b) Defect-rich muscovite packet between two kaolinite packets. (c) Kaolinite-rich area with relic thin packets of muscovite. (d) Bent and broken chlorite crystals containing aggregates of poorly crystalline material along the cleavage planes. (e) Almost entirely undeformed chlorite packets. (f) Aggregates of unoriented packets of poorly crystalline material located between fractured phyllosilicate grains. (g) Semi-ordered aggregates of partially oriented packets including kaolinite, Al-smectite and fine-grained muscovite. (h) Muscovite packet from a semi-ordered aggregate with a 20 Å periodicity. Mineral abbreviations according to Kretz (1983).

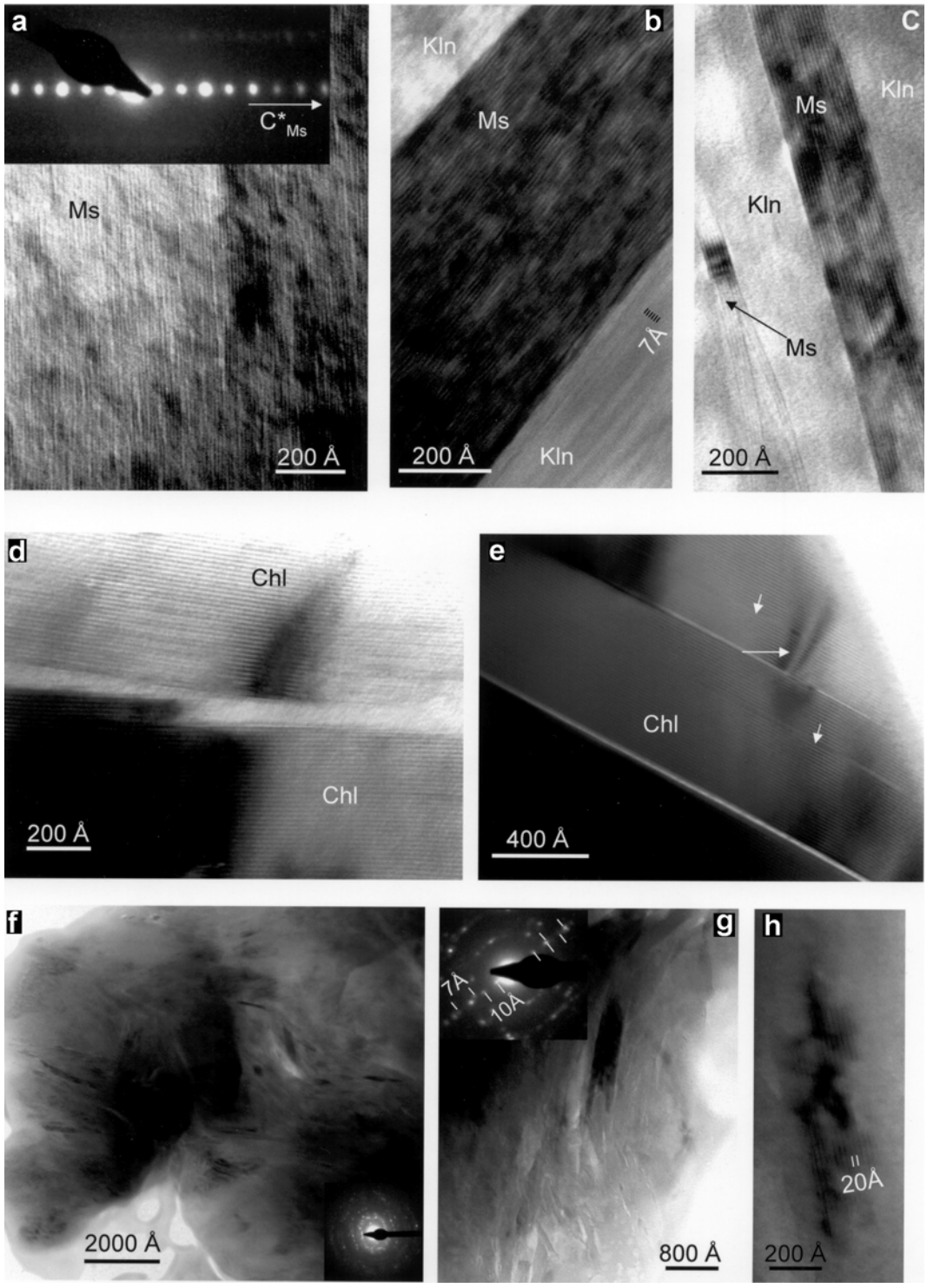
a
C*Ms
Ms
200 Å
b
Kln
Ms
7Å
200 Å
Kln
C
Ms
Kln
Kln
Ms
200 Å
d
Chl
Chl
200 Å
e
Chl
400 Å
f
2000 Å
g
7Å
10Å
800 Å
h
20Å
200 Å

TABLE 5. Whole-rock analyses of major elements (oxide wt.%).

Samples	SiO_2	Al_2O_3	CaO	MgO	Na_2O	K_2O	Fe_2O_3	FeO	MnO	TiO_2	P_2O_5	LOI
Eastern basin												
ST-5	61.91	17.91	0.14	2.24	2.41	3.04	2.45	4.27	0.04	0.90	0.12	3.50
ST-7	62.51	15.65	0.23	1.9	2.68	2.84	0.76	6.00	0.07	0.76	0.12	5.30
ST-8	56.17	18.27	0.31	2.16	2.31	3.91	2.60	4.62	0.07	0.85	0.19	7.40
ST-9	60.85	17.56	0.22	2.07	2.49	3.32	2.05	4.56	0.06	0.83	0.13	5.00
ST-10	56.80	20.06	0.26	1.63	2.72	4.23	1.52	4.05	0.05	0.92	0.16	6.40
ST-13	62.13	15.38	0.54	2.10	2.17	3.4	2.04	4.36	0.08	0.73	0.17	6.50
ST-16	60.00	20.65	0.35	1.54	0.71	2.9	2.47	5.55	0.10	0.82	0.13	3.60
ST-17	49.18	24.58	0.35	2.08	0.83	5.09	5.06	5.17	0.31	1.04	0.09	5.10
ST-18	49.75	26.09	0.26	1.89	1.23	4.72	2.27	6.63	0.16	1.09	0.15	4.60
ST-19	52.01	22.97	0.24	1.95	0.71	5.05	3.37	5.40	0.14	1.07	0.17	5.50
ST-20	68.41	12.17	0.36	1.40	1.36	1.87	1.41	4.85	0.18	0.73	0.12	6.10
Western basin												
SV-6	56.76	20.94	0.03	2.23	0.34	3.16	4.23	5.44	0.10	1.10	0.10	5.20
SV-7	70.16	13.38	0.13	1.53	0.77	2.25	2.72	3.91	0.06	0.79	0.12	2.90
SV-8	58.43	20.27	0.11	1.99	0.78	3.83	2.83	5.75	0.12	0.76	0.10	3.80
SV-9	54.40	22.13	0.18	2.17	1.61	3.94	4.00	5.21	0.11	0.97	0.12	4.00
SV-10	51.57	24.50	0.15	2.16	1.59	4.77	1.99	6.51	0.09	0.99	0.12	4.40
SV-11	56.52	13.38	0.64	3.82	0.36	0.44	8.98	9.10	0.36	0.55	0.48	4.10
SV-12	52.48	23.23	0.24	2.24	1.37	4.52	4.35	4.91	0.14	0.93	0.20	4.20
SV-13	51.66	24.73	0.13	1.98	1.34	5.03	5.16	2.98	0.10	1.03	0.11	4.40
SV-14	56.27	21.51	0.32	2.19	0.80	4.25	4.70	4.28	0.12	0.94	0.16	4.10
SV-15	50.28	26.27	0.12	1.99	0.97	5.10	2.50	5.63	0.09	1.25	0.12	4.50
SV-16	50.04	25.48	0.21	2.24	1.11	4.59	2.26	7.39	0.13	0.95	0.18	4.40
SV-17	56.05	24.24	0.04	1.44	0.8	5.00	0.01	5.72	0.06	0.94	0.10	4.20
PAAS*	62.80	18.90	1.30	2.20	1.20	3.70	–	6.50	0.11	1.00	0.16	6.00

* Average post-Archaean Australian shales (Taylor & MacLennan, 1985)LOI: loss on ignition

phengitic substitution (Fig. 8a). According to Abad *et al.* (2006) the illitic component becomes insignificant for the epizonal samples and in this case, all analyses belong to epizonal samples and show an interlayer charge population of >0.8 a.p.f.u.

In addition, the Na content is generally low (<0.25 a.p.f.u. in the western basin micas and <0.15 a.p.f.u. in the eastern basin micas), and therefore, paragonitic substitution (not shown) is not a significant compositional vector in these samples either. Albite, which is present as a metamorphic phase, must be responsible for both the lack of paragonite as a discrete phase and the scarcity of paragonitic substitution in the white micas. Mn and Ca (also analysed) are not included in the data table as they are present in proportions of $\leqslant 0.03$ a.p.f.u.

Trioctahedral chlorites have been analysed by SEM/EDX and TEM/AEM (Table 4). Western basin chlorites correspond to chamosite variety and eastern basin chlorites to clinochlore. Fe/(Fe+Mg) ratios are within the range of values characteristic of chlorites in low-grade metamorphic rocks and are very constant in both sequences, with larger values in the western basin chlorites (Fe/(Fe+Mg) = 0.60−0.72) than those in the eastern basin (Fe/(Fe+Mg) = 0.42−0.51).

Kaolin (Table 3) shows, according to the AEM analyses, an Al-rich composition, with small quantities of Fe and Mg (<0.18 a.p.f.u.), K and Na (<0.24 a.p.f.u.), the latter may be due to the contamination with other phases, such as illite or muscovite. Feldspars display a composition near to the end-member albite.

In addition, as has been described above, western basin slates contain carbonates with compositions near to siderite with some magnesitic component ($Fe_{0.73}Mg_{0.25}Ca_{0.02}CO_3$), according to the SEM/EDX analyses.

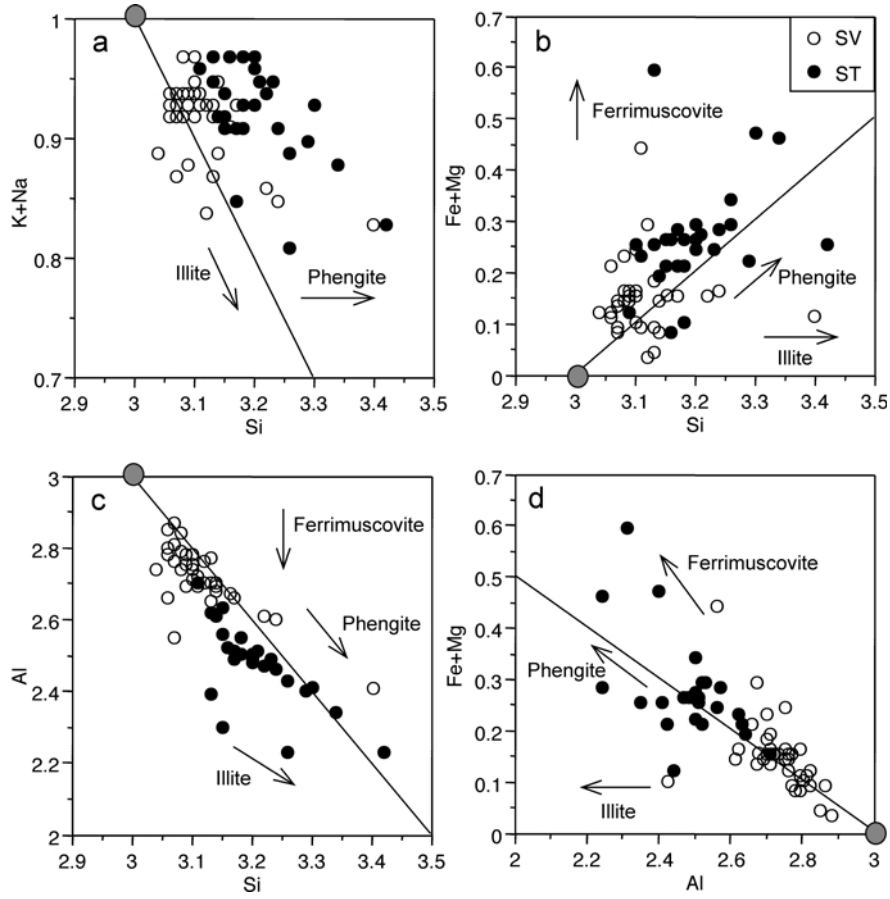

FIG. 8. Chemical composition diagrams of micas of the studied samples. Open circles: western basin samples; solid circles: eastern basin samples.

Whole-rock chemical composition

Table 5 shows the results of the chemical analyses of the rocks studied and the average of post-Archaean Australian Shales (PAAS, Taylor & McLennan, 1985) for comparison. The most significant difference observed between the samples of each basin is that the Fe content is commonly higher in the western basin slates (average of 7.41% FeO + Fe_2O_3) than in the eastern basin samples (average of 9.21% of FeO + Fe_2O_3). Some slates from the eastern basin are enriched in Na_2O (up to 2.72%) which is related to the presence of significant amounts of albite.

DISCUSSION AND CONCLUSIONS

This mineralogical and petrological study provides data on which to base a tectonometamorphic model applicable to the generation of small low-grade metamorphic terranes within major transform zones. Moreover, our results can contribute to an improved understanding of the shear deformation-metamorphism interaction processes that have taken place during the evolution of the Ossa-Morena Zone affected by the Porto–Coimbra–Tomar shear band (Fig. 9).

Prograde low-grade metamorphism characterization and geotectonic setting

Based on the KI values of white micas, these areas have undergone metamorphic conditions of high anchizone and epizone (KI <0.30Δº2θ). This is in accordance with the mineral assemblages of samples and the population of the illite polytypes from both basins which suggest a metamorphic

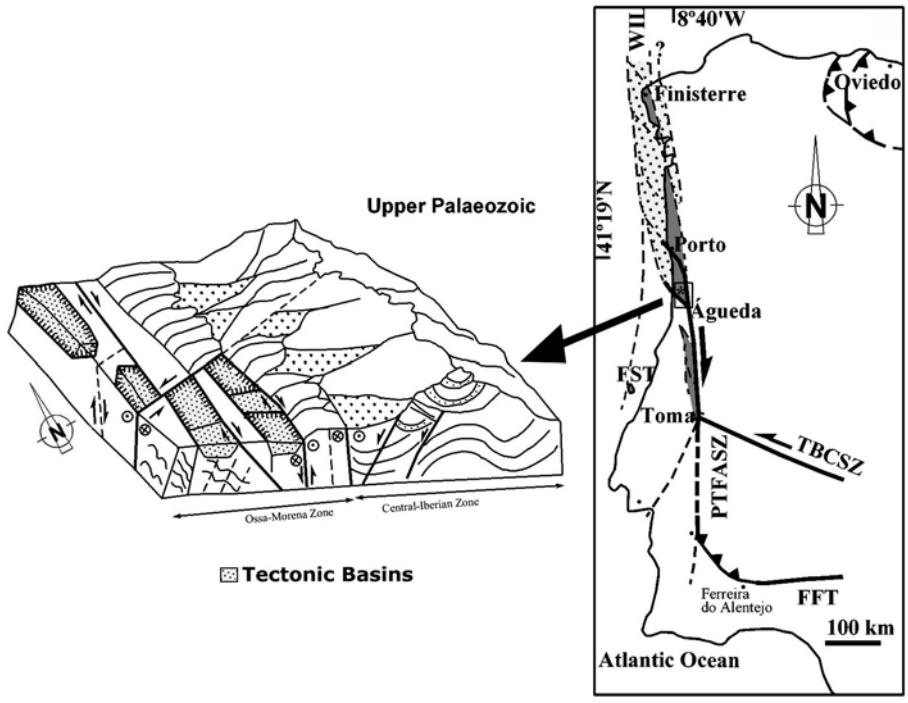

FIG. 9. Schematic diagram illustrating the geodynamic framework of Upper Palaeozoic basins *vs*. Proterozoic substratum fracture patterns on the Espinho–Albergaria-a-Velha metamorphic belt (Ossa-Morena Zone) during Upper Palaeozoic times (adapted from Chaminé *et al.*, 2006). WIL: Western Iberian Line, PTFASZ: Porto–Tomar–Ferreira do Alentejo major shear zone, FFT: Ferreira do Alentejo–Ficalho thrust, TBCSZ: Tomar–Badajoz-Córdoba shear zone, FST: Farilhões suspect terrane.

temperature >200ºC (Merriman & Peacor, 1999; Merriman & Frey, 1999). In relation to the *b* values, they do not show any correlation with the basal spacing, being, in general, both small and without significant differences among samples or fractions (Table 1). The low phengitic content of the K-rich micas, as deduced from the *b* parameter (8.967–9.015) Å and EDX analyses (Table 2), is characteristic of low-pressure regional metamorphism (1–2 kbar) according to Guidotti & Sassi (1986) although in detail, the phengitic content of the eastern basin K-micas is slightly greater than in the western basin K-micas. According to Merriman & Frey (1999) the geotectonic setting can be related to the *P-T* conditions estimated. In these Upper Paleozoic basins, the temperatures deduced from the KI values and index minerals (>200ºC) and the low pressures deduced from the *b* parameter and phengitic contents (1–2 kbar) can be related to an extensional geotectonic setting. This is in accordance with Chaminé *et al.* (2003b, 2006), who, based on geotectonic and biostratigraphic data, interpreted these tectonic basins as suggested pull-apart areas formed in an extensional regime related to the shear zone activity. Long-lived transform zones are prone to alternating local compression and extension. Periodic closure of pull-apart basins, formed within such zones, can cause formation of small low-grade metamorphic terranes included in a crystalline substratum of higher metamorphic grade. Dempster & Bluck (1995) interpreted some blocks of the Scottish Highlands as examples of such low-grade metamorphic terranes generated during the prolonged break-up of the Rodinia supercontinent with major strike-slip zone activity.

In the present study area, slates of epizonal grade from the pull-apart basins are included in a higher metamorphic grade substratum. This substratum is made of rocks affected by the first main stage of Variscan tectonometamorphism, which sometimes overprints an earlier Cadomian high-grade blasto-mylonitic fabric (Chaminé, 2000; Chaminé *et al.*, 2003a). Epizone conditions deduced from the

studied basins could have been reached as a consequence of the thickening produced by the internal sediment pile growth of the basin and the imbrication with the substratum materials. Therefore, the established metamorphic conditions for the studied materials could correspond to the second regional tectonometamorphic main stage of Variscan deformation associated with the presence of mega-shear zones described by Dias & Ribeiro (1993, 1995), Chaminé *et al.* (2003b, 2006) and Gutiérrez-Alonso *et al.* (2004) among others.

The large size, homogeneity and well crystallized aspect of K-mica and chlorite grains in the lattice-fringe images (Figs 6, 7) confirm their stability in this low-grade environment. The compositions show an almost complete lack of illitic substitution, which is characteristic of the epizonal samples (Abad *et al.*, 2006).

Chlorite compositions have not been used to characterize the low-grade conditions. The presence of chlorite in all samples is due to the high Fe+Mg content in the bulk-rock compositions (Table 5). In addition, the chlorite compositions are in accordance with the chemical compositions of the respective rocks. For example, sample ST13 contains chlorites with lower Fe/(Fe+Mg) than sample SV6 (0.45 and 0.60, respectively), which can be correlated with this chemical parameter in both rocks (0.67 and 0.71, respectively). Eastern basin chlorites also show smaller *b* parameters than the western basin ones. Although the ^{IV}Al content of chlorite was proposed as a geothermometer in low-temperature environments (Cathelineau & Nieva, 1985) it is well known that the composition of the rocks can be a decisive factor in the composition of chlorites (Bevins *et al.*, 1991; López-Munguira *et al*., 2002). In those cases, chlorites cannot be used as geothermometers (Zane *et al.*, 1998).

Effects related to the shear-zone activity

The XRD, SEM and TEM studies performed on the black slates from the tectonic basins associated with the Porto–Coimbra–Tomar shear zone have allowed us to deduce that some of their features are the result of tectonic and fluid-rock interaction processes.

Deformation intensity. Textural data reveal variations in deformation intensity between materials from both basins. The low density of crystal defects as well as the rare presence of nanometric folds and brittle fractures reveals textures indicative of high degrees of deformation are lacking in the western basin phyllosilicates. On the other hand, optical and BSE images show a dense fracture network filled by carbonates and clay minerals in slates from the eastern basin. Moreover, TEM textural data suggest that the epizonal phyllosilicates from the eastern basin were more intensely affected by deformation. A high degree of deformation in muscovite from this basin is indicated by the common presence of crystal dislocations, mottling and the development of micropackets with low-angle boundaries. Merriman *et al.* (1995) indicated that in highly strained muscovite grains, stacks of subgrains can be developed by strain-induced slip along (001) planes. Strain-induced features are well developed on chlorites from the eastern basin. In these chlorites, deformation is responsible for bending, fracturing and the presence of voids between packets. The predominance of brittle textures indicates that deformation was developed under low-*T*, and non-metamorphic conditions.

Retrograde crystallization stage. A correlation between deformation intensity and the extent of the presence of siderite, kaolin group minerals and Al-smectite can be established. This correlation suggests that deformation was the prime control for the development and superimposition of a retrograde carbonate and phyllosilicate association on the prograde epizonal metamorphic paragenesis. Fracturing during cataclastic flow, produced by shear zone activity, probably generated permeability, which allowed the circulation of lower-*T* fluids that replaced the pre-existing association and the injection and percolation of metasomatic carbonates.

The presence of siderite veins in the eastern basin rocks show an initial retrograding path environment, related to the circulation of hot metamorphic waters rich in CO_2, along the fractures associated with the shear activity. According to Mateus *et al.* (1999), this process could be mainly assigned to large-scale and repeated H_2O, CO_2 and (subordinate) SiO_2 introduction into the system through the main shear zones, in our case, through NNW–SSE dextral vertical shear zones. This large-volume, extremely well focused, fluid inflow generally induced the carbonization of the adjoining rocks. The origin of these fluids is believed to be related mainly to degassing processes during the second regional stage of Variscan deformation resulting in

metamorphic blastesis and metasomatism (Chaminé, 2000).

In addition, dickite has been described as white concentrations, frequently in veinlets of the eastern basin metacarbonates and slates close to fractures related to the shear zone. This double layer polytype of the kaolin group is considered to be a relatively high-*T* mineral (Keller, 1988). The genesis of this polytype must be related to the continuous circulation of hot metamorphic waters along the shear zones with the subsequently hydrothermal alteration. Its location (filling distensive zones) and texture (random aggregates) suggest a post-kinematic origin.

Finally, the retrograde process culminated in the crystallization of kaolin and Al-smectite favoured by the circulation of low-*T* waters along the rocks. Several authors have interpreted the presence of kaolinite and smectite in this kind of sequence as the result of 'retrograde diagenesis' (e.g. Nieto *et al.*, 2005 and references therein). Transmission electron microscopy textures show that dioctahedral smectite in the eastern basin slates is derived through replacement of trioctahedral chlorite. Chlorite shows signs of alteration and has some compositions corresponding to different degrees of smectite contamination. Similar compositional effects were described as the result of retrograde alteration by Nieto *et al.* (1994).

Summarizing the influence of deformation in the alteration of clay minerals, we argue that HRTEM and BSE images and AEM-SEM analytical data reveal that only the retrograde clay mineral reactions in the eastern basin are strongly associated with the microtextural evidence of deformation. In several samples of this basin, deformation is responsible for the intense mottled appearance of muscovite grains containing dislocations, layer disruption and low-angle boundaries among thin micropackets. Deformation also produced bent and broken chlorite grains with irregular edges containing lattice fringes disrupted and imbricated. Strongly deformed grains usually contain aggregates of poorly-crystalline material along the cleavage where kaolin, and Al-smectite appear. Active deformation can enhance the diffusion process within the phyllosilicate grains promoting metamorphic reactions. The diffusion mechanisms can be affected by the introduction of lattice defects and the development of microcavities allowing a fluid to permeate and effectively permit transport processes to operate. We consider that the microcavities observed in the phyllosilicate grains from the eastern basin can act as potential channels for transport of fluids and serve as sites for the beginning of alteration. Therefore, we suggest that the occurrence of aggregates of kaolin, Al-smectite and fine-grained muscovite is probably related to retrograde metamorphism, along micro-fractures that formed during deformation. In the strongly deformed areas, an intense fluid-rock interaction under low-*T* conditions produced the intense alteration of the previous phyllosilicates, which only appear as relict thin packets.

ACKNOWLEDGMENTS

Financial support was provided by the Research Project nº BTE2003-07867 and the 'Acción Integrada Hispano-Portuguesa' HP2003-0074 both of the Spanish Ministry of Science and Technology, a postdoctoral grant to M.V.V. of the Spanish Ministry of Education and Culture and Research Group RNM-325 of the Junta de Andalucía. This research was also partially supported by R&D Projects granted by the Portuguese Foundation for Science and Technology (FCT) and FEDER EU funds, contracts Geodyn (POCTI-ISFL-5-32/Lisbon), FCT-SFRH/BPD/3641/2000 (HIC, Aveiro), MODELIB (POCTI-35630/CTA/2000-FEDER) and GROUNDURBAN (POCTI/CTE-GIN/59081/2004). We are grateful to P. Árkai, B. Bauluz and an anonymous reviewer for their helpful comments and suggestions.

REFERENCES

Abad I., Nieto F., Gutiérrez-Alonso G., Do Campo M., López-Munguira A. & Velilla N. (2005) Illitic substitution in micas of very low-grade metamorphic clastic rocks. *European Journal of Mineralogy*, **18**, 59–69.

Arkai P., Mahlmann R.F., Suchy V., Balogh K., Sykorova I. & Frey M. (2002) Possible effects of tectonic shear strain on phyllosilicates: a case study from the Kandersteg area, Helvetic domain, Central Alps, Switzerland. *Schweizerische Mineralogische und Petrographische Mitteilungen*, **82**, 273–290.

Bailey S.W. (1980) Structures of layer silicates. Pp. 1–123 in: *Crystal Structures of Clay Minerals and their X-ray Identification* (G.E. Brindley & G. Brown, editors). Monograph, **5**, Mineralogical Society London, UK.

Beetsma J.J. (1995) *The late Proterozoic/Paleozoic and Hercynian crustal evolution of the Iberian Massif, N Portugal, as traced by geochemistry and Sr-Nd-Pb isotope systematics of pre-Hercynian terrigenous*

sediments and Hercynian granitoids. PhD thesis, Vrije Universiteit, Amsterdam, Holland.

Bevins R.E., Robinson D. & Rowbotham G. (1991) Compositional variations in mafic phyllosilicates from regional low-grade metabasites and application of the chlorite geothermometer. *Journal of Metamorphic Geology*, **9**, 711–721.

Caillère S., Henin S. & Rautureau M. (1982) Minéralogie des argiles. *Acte Scientifique Agricol de L'I.N.R.A 8.* Masson, Paris.

Cathelineau M. & Nieva D. (1985) A chlorite solid solution geothermometer: the Los Azufres (Mexico) geothermal system. *Contributions to Mineralogy and Petrology*, **91**, 235–244.

Chaminé H.I. (2000) *Estratigrafia e estrutura da faixa metamórfica de Espinho-Albergaria-a-Velha (Zona de Ossa-Morena): implicações geodinâmicas*. PhD thesis, Universidade do Porto, Portugal.

Chaminé H.I., Gama Pereira L.C., Fonseca P.E., Noronha F. & Lemos de Sousa M.J. (2003a) Tectonoestratigrafia da faixa de cisalhamento de Porto–Albergaria-a-Velha–Coimbra–Tomar, entre as Zonas Centro-Ibérica e de Ossa-Morena (Maciço Ibérico, W de Portugal). *Cadernos do Laboratorio Xeolóxico de Laxe, A Coruña*, **28**, 37–78.

Chaminé H.I., Gama Pereira L.C., Fonseca P.E., Moço L.P., Fernandes J.P., Rocha F.T., Flores D., Pinto de Jesus A., Gomes C., Soares de Andrade A. & Araújo A. (2003b) Tectonostratigraphy of middle and Upper Palaeozoic black shales from the Porto–Tomar–Ferreira do Alentejo shear zone (W Portugal): new perspectives on the Iberian Massif. *Geobios*, **36**, 649–663.

Chaminé H.I., Fonseca P.E., Pinto de Jesus A., Gama Pereira L.C., Fernandes J.P., Flores D., Moço L.P., Castro R.D., Gomes A., Teixeira J., Araújo M.A., Soares de Andrade A.A., Gomes C. & Rocha F.T. (2006) Tectonostratigraphic imbrications along strike-slip major shear zones: an example from the early Carboniferous of SW European Variscides (Ossa-Morena Zone, Portugal). In: *Proceedings of the XVth International Congress on Carboniferous and Permian Stratigraphy (Utrecht, 2003)* (T.E. Wong, editor). Special Volume of the Royal Netherlands Academy of Arts and Sciences (in press), Netherlands.

Dempster T.J. & Bluck B.J. (1995) Regional metamorphism in transform zones during super continent breakup-Late proterozoic events of the Scottish highlands. *Geology*, **23**, 991–994.

Dias R. & Ribeiro A. (1993) Porto-Tomar shear zone, a major structure since the beginning of the variscan orogeny. *Comunicações Instituto Geológico Mineiro, Lisboa*, **79**, 31–40.

Dias R. & Ribeiro A. (1995) The Ibero-Armorican arc: a collision effect against an irregular continent? *Tectonophysics*, **246**, 113–128.

Do Campo M. & Nieto F. (2003) Transmission electron microscopy study of very low-grade metamorphic evolution in Neoproterozoic pelites of the Puncoviscana formation (Cordillera Oriental, NW Argentina). *Clay Minerals*, **38**, 459–481.

Farmer V.C. (1974). The layer silicates. Pp. 331–365 in: *The Infrared Spectra of Minerals* (V.C. Farmer, editor). Mineralogical Society of London, UK.

Fernandes J.P., Flores D., Rocha F.T., Gomes C., Gama Pereira L.C., Fonseca P.E. & Chaminé H.I. (2001) Devonian and Carboniferous palynomorph assemblages of black shales from the Ovar–Albergaria-a-Velha–Coimbra–Tomar (W Portugal): tectonostratigraphic implications for the Iberian Terrane. *Geociências, Revue de la Universiade de Aveiro*, **15**, 1–23.

Fernández F.J., Chaminé H.I., Fonseca P.E., Munhá J.M., Ribeiro A., Aller J., Fuertes-Fuentes M. & Borges F.S. (2003) HT-fabrics in a garnet-bearing quartzite from Western Portugal: geodynamic implications for the Iberian Variscan Belt. *Terra Nova*, **15**, 96–103.

Gama Pereira L.C. (1987) *Tipologia e evolução da sutura entre a Zona Centro Ibérica e a Zona Ossa Morena no sector entre Alvaiázere e Figueiró dos Vinhos (Portugal Central)*. PhD Thesis, Universidade de Coimbra, Portugal.

Gomes A., Chaminé H.I., Teixeira J., Fonseca P.E., Gama Pereira L.C., Pinto de Jesus A., Pérez Albertí A., Araújo M.A., Coelho A., Soares de Andrade A. & Rocha F.T. (2006) Late Cenozoic basin opening in relation to major strike-slip faulting along the Porto-Coimbra-Tomar fault zone (Northern Portugal). In: *Sedimentation and Tectonics: The Peter Friend Volume* (C. Paola, G. Nichols and E. Williams, editors). IAS Special Publication (in press).

Guidotti C.V. & Sassi F.P. (1986) Classification and correlation of metamorphic facies series by means of muscovite b data from low-grade metapelites. *Neues Jahrbuch für Mineralogie Abhandlungen*, **153**, 363–380.

Guidotti C.V, Yates M.G., Dyar M.D. & Taylor M.E. (1994) Petrogenetic implications of the Fe^{3+} content of muscovite in pelitic schists. *American Mineralogist*, **79**, 793–795.

Gutiérrez-Alonso G., Fernández-Suárez J. & Weil A.B. (2004) Orocline triggered lithospheric delamination. Pp. 121–130 in: *Orogenic Curvature, Integrating Paleomagnetic and Structural Analyses* (A.J. Sussman & A.B. Weil, editors). Special Paper, **383**, Geological Society of America, Boulder, Colorado.

Inoue A., Meunier A. & Beaufort D. (2004) Illite-smectite mixed-layer minerals in felsic volcaniclastic rocks from drill cores in Kakkonda Japan. *Clays and Clay Minerals*, **52**, 66–84.

Julivert M., Fontboté J.M., Ribeiro A. & Conde L.E.N. (1974) Mapa Tectónico de la Península Ibérica y

Baleares, Escala 1:1000.000. *Memoria Explicativa*, Instituto Geologico y Minero de España, Madrid. 113 pp.

Keller W.D. (1988) Authigenic kaolinite and dickite associated with metal sulfides. *Clays and Clay Minerals*, **36**, 153–158.

Kemp S.J., Merriman R.J. & Bouch J.E. (2005) Clay mineral reaction progress – the maturity and burial history of the Lias Group of England and Wales. *Clay Minerals*, **40**, 43–61.

Kisch H.J. (1991) Illite crystallinity: recommendations on sample preparation, X-ray diffraction settings, and interlaboratory samples. *Journal of Metamorphic Geology*, **9**, 665–670.

Kisch H.J., Árkai P. & Brime C. (2004) On the calibration of the illite Kübler index (illite 'crystallinity'). *Schweizerische Mineralogische und Petrographische Mitteilungen*, **84**, 323–331.

Kretz R. (1983) Symbols for rock-forming minerals. *American Mineralogist*, **68**, 277–279.

López-Munguira A., Nieto F. & Morata D. (2002) Chlorite composition controlled by whole-rock geochemistry. An HRTEM/AEM-EMPA-XRD study in Cambrian basic volcanic rocks from the Ossa Morena Zone, SW Spain. *Clay Minerals*, **37**, 267–281.

Lotze F. (1945) Zur Gliederung der Varisziden der Iberischen Meseta. *Geotektonische Forschungen, Berlin*, **6**, 78–92.

Mateus A., Figueiras J., Gonçalves M. & Fonseca P. E. (1999) Evolving fluid circulation within the Beja-Acebuches Variscan Ophiolite Complex (SE, Portugal). *Ofioliti*, **24**, 269–282.

Merriman R.J. & Frey M. (1999) Patterns of very low-grade metamorphism in metapelitic rocks. Pp. 61–107 in: *Low Grade-Metamorphism* (M. Frey & D. Robinson, editors). Blackwell Science, Oxford, UK.

Merriman R.J. & Peacor D.R. (1999) Very low-grade metapelites: mineralogy, microfabrics and measuring reaction progress. Pp. 10–60 in: *Low Grade-Metamorphism* (M. Frey & D. Robinson, editors). Blackwell Science, Oxford, UK.

Merriman R.J., Roberts B., Peacor D.R. & Hirons S.R (1995) Strain related differences in the crystal growth of white mica and chlorite: a TEM and XRD study of the development of metapelitic microfabrics in the Southern Uplands thrust terrain, Scotland. *Journal of Metamorphic Geology*, **13**, 559–576.

Moço L.P., Chaminé H.I., Fernandes J.P., Lemos de Sousa M.J., Fonseca P.E. & Ribeiro A. (2001) Organic metamorphism level of Devonian black shale from Albergaria-a-Velha region (NW Portugal): Tectonostratigraphic implications. *Gaia (Revue Museo Historia Naturelle, Lisboa)*, **16**, 195–197.

Nieto F. (2002) Characterization of coexisting NH_4- and K-micas in very low-grade metapelites. *American Mineralogist*, **87**, 205–216.

Nieto F., Velilla N., Peacor D.R. & Ortega-Huertas M. (1994) Regional retrograde alteration of sub-greenschist facies chlorite to smectite. *Contributions to Mineralogy and Petrology*, **115**, 243–252.

Nieto F., Mata P., Bauluz B., Giorgetti G., Árkai P. & Peacor D.R. (2005) Retrograde diagenesis, a widespread process on a regional scale. *Clay Minerals*, **40**, 93–104.

Oliveira A., Rocha F.T., Rodrigues A., Jouanneau J., Dias J.A., Weber O. & Gomes C. (2002) Clay minerals of the sedimentary cover from the Northwestern Iberian shelf. *Progress in Oceanography*, **52**, 233–247.

Ribeiro A., Quesada C. & Dallmeyer R.D. (1990) Geodynamic evolution of the Iberian Massif. Pp. 397–410 in: *Pre-Mesozoic Geology of Iberia* (R.D. Dallmeyer & E. Martínez-García, editors). Springer Verlag, Berlin.

Ribeiro A., Marcos A., Pereira E., Llana-Fúnez S., Farías P., Fernandéz F.J., Fonseca P.E., Chaminé H.I. & Rosas F. (2003) 3-D strain distribution in the Ibero-Armorican Arc: a review. *Ciências da Terra*, UNL, Lisboa, Nº Esp. 5 (CD-Rom), D62–D63.

Robinson D., Schmidt S.T. & de Zamora A.S. (2002) Reaction pathways and reaction progress for the smectite-to-chlorite transformation: evidence from hydrothermally altered metabasites. *Journal of Metamorphic Geology*, **20**, 167–174.

Schleicher A.M., Warr L.N. & van der Pluijm B.A. (2006) Fluid focusing and back-reactions in the uplifted shoulder of the Rhine rift system: a clay mineral study along the Schauenburg Fault zone (Heidelberg, Germany). *International Journal of Earth Sciences*, **95**, 19–33.

Taylor S.R. & McLennan S.M. (1985) *The Continental Crust: its Composition and Evolution*. Blackwell, Oxford, UK, 312 pp.

Warr L.N. & Rice H.N. (1994) Interlaboratory standardization and calibration of clay mineral crystallinity and crystallite size data. *Journal of Metamorphic Geology*, **12**, 141–152.

Zane A., Sassi R. & Guidotti C.V. (1998) New data on metamorphic chlorite as a petrogenetic indicator mineral, with special regard to greenschist-facies rocks. *The Canadian Mineralogist*, **36**, 713–726.